The following article appeared in *Nano Lett.*, **2018**, *18* (4), 2304–2310 and may be found at https://pubs.acs.org/doi/abs/10.1021/acs.nanolett.7b05015

Single-mode Near-infrared Lasing in a GaAsSb-based Nanowire Superlattice at Room Temperature

Dingding Ren[1], Lyubomir Ahtapodov[1], Julie S. Nilsen[2], Jianfeng Yang[3], Anders Gustafsson[4], Junghwan Huh[1], Gavin J. Conibeer[3], Antonius T.J. van Helvoort[2], Bjørn-Ove Fimland[1], and Helge Weman[1]

[1] Department of Electronic Systems and [2] Department of Physics, Norwegian University of Science and Technology (NTNU), NO-7491 Trondheim, Norway

[3] Australian Centre for Advanced Photovoltaics, University of New South Wales, Sydney, New South Wales 2052, Australia

[4] Solid State Physics and NanoLund, Lund University, Box 118, SE-22100 Lund, Sweden

Keywords: nanowire laser; GaAsSb; superlattice; molecular beam epitaxy

Abstract: Semiconductor nanowire lasers can produce guided coherent light emission with miniaturized geometry, bringing about new possibilities for a variety of applications including nanophotonic circuits, optical sensing, and on-chip and chip-to-chip optical communications. Here, we report on the realization of single-mode and room-temperature lasing from 890 nm to 990 nm utilizing a novel design of single nanowires with GaAsSb-based multiple axial superlattices as gain medium under optical pumping. The control of lasing wavelength via compositional tuning with excellent room-temperature lasing performance is shown to result from the unique nanowire structure with efficient gain material, which delivers a low lasing threshold of ~ 6 kW/cm^2 (75 μJ/cm^2 per pulse), a lasing quality factor as high as 1250 and a high characteristic temperature of ~ 129 K. These results present a major advancement for the design and synthesis of nanowire laser structures, which can pave the way towards future nanoscale integrated optoelectronic systems with superior performance.

Semiconductor nanowire (NW) lasers can produce nanoscale localized coherent light emission for a variety of laser applications from biomedical sciences to information technology.[1–3] The large effective refractive index of semiconductor NWs with diameters in the range of a few hundred nanometers allows for strong optical modal confinement in the radial direction, and the coherent light is extracted out directionally from micrometers long NW Fabry–Pérot (FP) cavities, which is distinct from other types of nanolasers.[4–8] Proof-of-principle NW lasers based on bulk[1], core-shell[9] and dots-in-wire[10] gain structures have been developed to realize lasing. However, it is still challenging for NW lasers to achieve lasing emission at longer wavelengths in the near-infrared at room temperature, which is needed for optical interconnects in future compact nanophotonic circuits and on-chip communication systems and for bio-medical applications. Thus, an alternative NW heterostructure architecture that enables room-temperature lasing at the longer near-infrared

wavelengths, e.g. 980 nm for Er-doped fibre optical amplifiers[11] and efficient tissue ablation for clinical surgeries[12], is highly demanded.

To date, FP NW laser structures with ZnO[1] and ZnS[13] for ultraviolet, III-nitride[2,14] for visible, and GaSb[15], GaAs[16,17] and III-P[18] for near-infrared lasing have been demonstrated. NW lasers with binary semiconductor bulk gain are straightforward to synthesize, but achieving low lasing threshold, high lasing quality factor and wide wavelength tunability is much more challenging. This will require incorporation of controllable and complex low-dimensional heterostructures within the NW.[19] Specifically in the near-infrared region, demonstrated lasing emission from NWs with radial core-shell quantum wells are predominantly at, or close to, the bandgap of the binary core,[20–22] possibly due to the challenges in achieving a homogeneous ternary shell.[23] In current axial heterostructured NWs, e.g. quantum dots-in-wire structures, the available states for radiative recombination are restricted by both the limited number of available states in one quantum dot and the limited number of quantum dots integrated within one NW. Again, this results in lasing close to the band gap of the binary core material.[10] Also, nanopillar-based lasers with InGaAs multi-quantum wells have only been shown to lase at low temperature.[24] Thus, an alternative NW laser architecture with both good wavelength tunability via compositional control and sufficient optical gain for single-mode lasing operation at room temperature is desired. Axial superlattices can be incorporated inside NW structures with high crystal quality[25,26] and provide an accumulatively long gain medium of lower bandgap material with a sufficient number of available states for radiative recombination, and may therefore be such an ideal NW laser structure.[27,28]

Here, we demonstrate single NW lasers with six GaAsSb-based multiple superlattices, each consisting of ten GaAsSb-rich inserts, as gain medium, synthesized by a position-controlled Ga self-catalyzed growth method. Single-mode lasing has been observed at room temperature from

890 nm to 990 nm by adjusting the Sb content in the superlattices, delivering a lasing quality factor as high as 1250 with high characteristic temperature of 129 K. In addition, the lasing threshold has also been reduced from ~ 12 kW cm^{-2} to ~ 6 kW cm^{-2} (75 μJ/cm^2 per pulse) with higher Sb content and deeper potential wells in the superlattices.

Recently, self-catalyzed GaAsSb NWs have demonstrated good optical emission tunability in the near-infrared region.[29–32] In this study, we have grown multiple GaAsSb-based superlattices in GaAs NWs, where such tunability is demonstrated in combination with good lasing performance at room temperature (i.e. high lasing quality-factor and predomantly single-mode). The NW laser is schematically designed and shown in Fig. 1a and b before the growth and characterization experiments. In the design, six GaAsSb-based superlattices are separated by GaAs spacers, and each superlattice contains ten superlattice periods of high Sb-content GaAsSb potential wells with low-Sb content GaAsSb barriers in between. Three different Sb composition profiles (samples A-C with increasing Sb content from A to C) were grown and investigated. The NW superlattice structures were grown by self-catalyzed molecular beam epitaxy (MBE) on Si(111) substrates with an electron beam lithography patterned thermal oxide mask, giving a high yield of uniform vertical NWs in a regular array, as shown in Fig. 1c and d (for growth details see the Methods). The bright-field transmission electron microscopy (BF-TEM) image in Fig. 1e shows a representative NW laser with a diameter of ~ 400 nm and a length of ~ 10 μm from sample B. To extract the compositional profile of the superlattices in the axial direction of the NW, we performed high-angle annular dark-field scanning TEM (HAADF-STEM) combined with energy dispersive x-ray (EDX) spectroscopy on a ca. 100 nm thick slice extracted from the center of a NW using focused ion beam (FIB) milling. As an example, the compositional profile of Sb in the fourth superlattice, marked by an orange rectangle in Fig. 1e, is presented in Fig. 1f based on EDX line scan

measurements. This "sawtooth" compositional profile shows that the Sb content varies periodically with a maximum nominal content of ~ 5 at. % (i.e. an Sb molar fraction of ~ 0.10), which leads to periodic triangular quantum wells for the holes along the NW axis (see Supplementary Section I). The Sb-profiles for all superlattices in NWs from all three batches are given in Supplementary Section II. In general, the Sb content builds up in the first superlattice and a stable triangular potential superlattice is formed from the second superlattice onwards. We emphasize here that both the high Sb solubility in the Ga catalyst and the reduction of supersaturation by the Sb incorporation in the GaAs NW lead to a reservoir effect.[29] Using a short-time supply of Sb flux, this reservoir effect results in the formation of relatively wide GaAsSb potential wells with gradually decreasing Sb content. Thereby severe radial growth induced compositional variations, i.e. GaAsSb shell formation, are minimized. Whereas some GaAs radial growth can be expected during the axial GaAs growth, this would only act as a potential barrier for the GaAsSb-based superlattice.

The optical characteristics of the as-grown vertical NW array in sample B have been examined by both cathodoluminescence (CL) and micro-photoluminescence (μ-PL) spectroscopy. Figure 1g shows the low-temperature (8 K) CL spectrum, and the spatially resolved CL map for emission in the 900 to 938 nm region (red colored regions) is overlaid with the corresponding cross-section SEM image, demonstrating that most of the light emission in this region comes from the six GaAsSb-based superlattices with a dominant peak at ~ 925 nm. The other two emission peaks at ~ 875 nm and ~ 820 nm, seen in the CL spectrum in Fig. 1g, can be found to originate from the GaAs spacers between the six superlattices and the GaAs tip in the false-color image Fig. 1h, respectively. Since the dominant emission intensity is from the six GaAsSb-based superlattices, this indicates that the GaAsSb-rich potential wells in the superlattices can efficiently capture the

photo-generated electron-hole pairs along the entire NW length, which then recombine via localized inter-subband transitions. In addition, we found periodic modulation of the spontaneous emission from the superlattices, as indicated by the red dashed lines in Fig. 1g. This periodic modulation of the emission is consistently observed along the entire NW from the spatial-resolved CL spectrum in Fig. S6, indicating the presence of FP modes inside the NW (see Supplementary Section IV). The room-temperature μ-PL spectrum from the as-grown vertical NW array shows a dominant emission at ~ 955 nm, as shown in Fig. 1i, which demonstrates that the superlattices are optically bright also at room temperature.

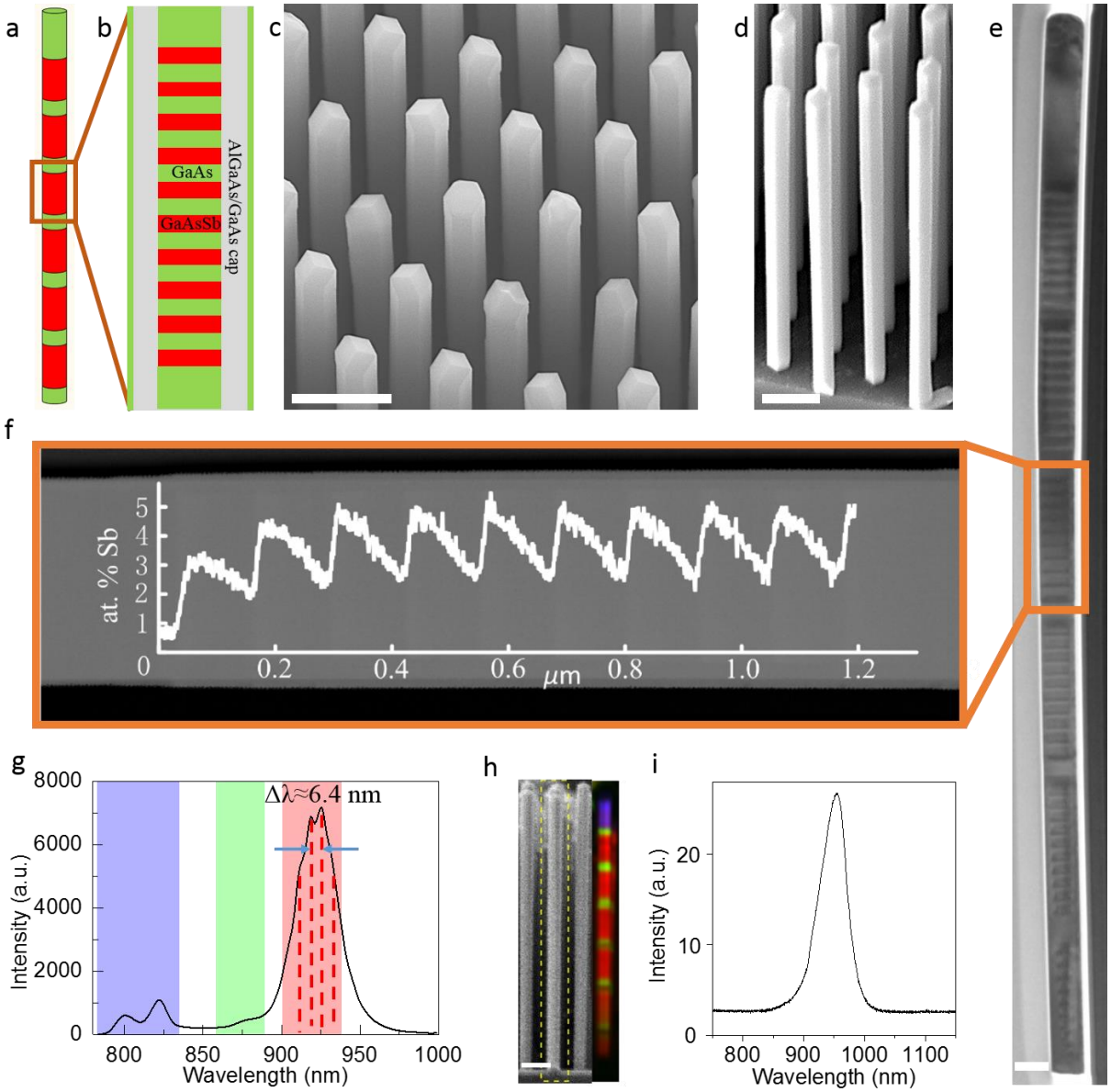

Figure 1. Structural and optical properties of the NW superlattice laser (sample B). a, Schematics of the NW consisting of six periodic GaAsSb-based superlattices (red) separated by GaAs spacers (green) and b, schematic design of each superlattice. c, d, 20° (c) and 30° (d) tilted-view SEM images of an as-grown NW array on a Si(111) substrate with an EBL patterned oxide mask, from the center and cleaved edge respectively. e, Cross-section BF-TEM image of a representative NW from (c). f, Cross-section HAADF-STEM with the correlated EDX Sb composition profile of the fourth NW superlattice, marked by the orange rectangle in (e). g,

Average low-temperature CL spectrum of the as-grown NW array with color coding for three different spectral regions as used to construct the CL false-color image in (h). The vertical red dashed lines represent the periodic peaks of the spontaneous emission originating from the FP modes of the NW laser cavity. h, Cross-section SEM image of the as-grown NWs and the corresponding low-temperature CL false-color image. i, Room-temperature μ-PL spectrum of the as-grown NW array at a pumping/excitation power density of 125 W cm^{-2}. The scale bars are 1 μm, 1 μm, 500 nm and 1 μm in (c), (d), (e) and (h), respectively.

A pulsed Ti:sapphire laser set to 800 nm was used for optical pumping experiments (see details in Methods section). Figure 2a shows a representative NW with a length of ~ 10 μm and a diameter of ~ 435 nm at the tip and ~ 395 nm at the bottom (i.e. slightly anti-tapered) from sample B. The emission spectra under pulsed excitation are shown in Fig. 2b. By increasing the excitation power density, a superlinear increase of the PL peak intensity at 950 nm is observed beyond ~ 6 kW cm^{-2} (75 μJ/cm^2 per pulse) that differentiates the spontaneous and stimulated emission regimes in the fitted integrated emission intensity vs. average pumping power density dependence (L-L curve). This pumping power density has been used as the lasing threshold, which is lower than for previously reported NW lasers with bulk or quantum dot structures.[10,17] The Gaussian function-fitted L-L curve is presented in Fig. 2c on a logarithmic scale. From this L-L curve, a spontaneous emission coupling factor β ~ 3.3×10^{-3} is estimated based on fitting the rate equation (see Supplementary Section IX).[10,16,24,33] A sudden reduction in the full width at half maximum (FWHM) to ~ 0.76 nm was observed at the lasing threshold, as indicated in the Gaussian fitted function shown in the inset of Fig. 2b. The lasing quality (Q) factor, $\lambda/\Delta\lambda$, is estimated to be ~ 1250. Such small FWHM and high Q factor has not been reported previously at room temperature in III-V NW lasers using bulk[16] or quantum dot[10] as gain medium. To further confirm the lasing

behavior, an optical image of the NW above the lasing threshold, is shown in Fig. 2d. The bright emission spots at both ends of the NW with a clear interference pattern are consistent with the finite-difference-time-domain (FDTD) simulated interference pattern (Fig. 2e). This is a proof of coherent light emission and a strong wave-guiding effect in the NW FP cavity. It should be noticed that emission through the NW sidewalls is quite weak compared to the lasing from the end facets, indicating a strong radial optical confinement with a relatively small proportion of waveguide leakage from the NW cavity. Figure 2f shows the normalized lasing spectra above threshold at various temperatures from room temperature to 10 K. The decrease of the lattice temperature results in a blue shift of the NW lasing peak from ~ 950 nm to ~ 883 nm, which is well below the bandgap of GaAs (marked as vertical black dashed lines) in the whole temperature range, showing that the lasing occurs in the GaAsSb-based NW superlattices. In addition to the non-linear increase of the PL intensity with higher power, we also observed that the spontaneous emission lifetime is reduced dramatically. The lifetime of the emerging lasing peak is shorter than the resolution limit of our experimental setup, which is around 13 ps (see Supplementary Section VI). These observations agree well with lasing behavior in the NW at high excitation power. A characteristic temperature as high as ~ 129 K is obtained by fitting the exponential function of the lasing threshold power vs. temperature to the data points in Fig. 2g. This is among the highest values of characteristic temperatures for III-V semiconductor NW lasers reported so far.[10,17] We note that optical pumping at 10 K gives a laser wavelength shift towards higher energy with increasing excitation power (see Supplementary Section VI), which is attributed to band filling effects at low temperature with a longer carrier lifetime and a minor thermal broadening effect. In general, ~ 75 % of the NW superlattice lasers present single-mode operation at room temperature, which reflects a well-repeated gain structure without significant gain variations between the individual

superlattices. We note however that when the NW laser is cooled well below room temperature, there is some signature of multi-mode lasing as a result of a shift of the gain spectra. E.g. as seen in Fig. 2f, at 200 K a second peak appears at the high-energy side, indicating that the gain spectra here overlap with two possible modes

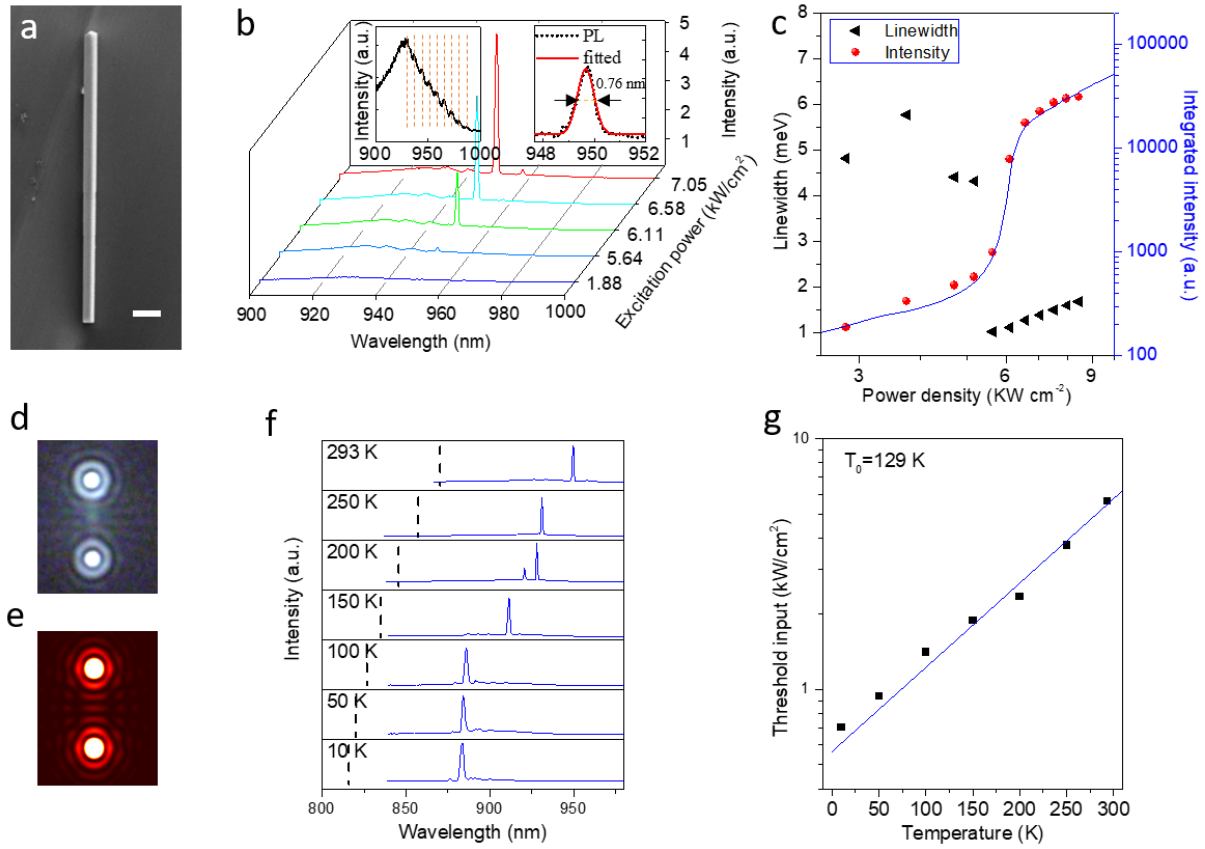

Figure 2. Lasing properties from a single NW superlattice laser (sample B). a, SEM image of a single NW superlattice placed on a SiO_2/Si substrate (scale bar 1 μm). b, Emission spectra at room temperature for a single NW laser under pulsed excitation at different power densities. The insets show a PL spectrum of equidistant FP modes below lasing threshold under a pumping power density of 1.88 kW/cm^2 and a Gaussian function fitted lasing peak with a FWHM ~ 0.76 nm from left to right, respectively. c, Double logarithmic L-L curve of integrated emission intensity and corresponding linewidth of the lasing peak vs. average optical pumping power

density at room temperature. d, Experimentally observed interference pattern from the NW laser above lasing threshold at room temperature. e, Corresponding FDTD-simulated interference pattern to (d). f, Temperature-dependent lasing emission spectra (normalized intensity) at temperatures from 10 K to 293 K. The vertical black dashed lines represent the wavelength corresponding to the GaAs bandgap, showing that the lasing from the GaAsSb-based superlattice is well below the GaAs bandgap energy (dashed lines). g, Plot of laser threshold pump power vs. temperature, indicating a fitted characteristic temperature of ~ 129 K.

To further evaluate the lasing properties from the NW superlattice laser, linear polarization emission measurements have been performed. The schematic of the NW principal axes and the PL spectra of orthogonal polarization detection are shown in Fig. 3a, and the intensity of the polarized PL emission from the NW as a function of the angle to the NW growth axis is shown in Fig. 3b. The degree of linear polarization, $(I_{\perp} - I_{\parallel})/(I_{\perp} + I_{\parallel})$, was determined to be 87 % for the NW laser shown in Fig. 2, based on a least-square fit to the experimental data. The lasing mode is thus strongly polarized perpendicularly to the NW axis (and the lineshape is Gaussian). Although the fundamental TE01 and HE11 modes separate from each other by ~ 1 meV (see Supplementary Section IV), we did not observe any extra or sub-modes/peaks from the polarization measurements, which indicates single-mode lasing. In addition, the samples with different Sb content show similar degree of polarization (~ 80 % to 90 %), and no Sb content-dependent relation to the polarization degree was found.

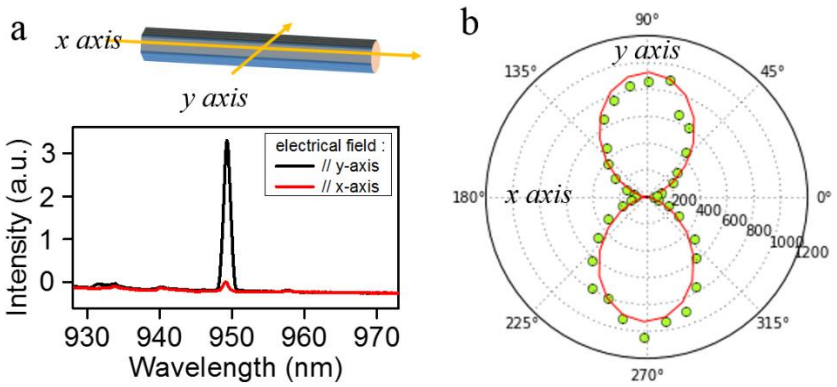

Figure 3. Polarization-dependent PL spectra of the NW superlattice lasing at room temperature just above threshold ~ 6 kW/cm^2 (the NW is shown in Fig. 2a from sample B) at room temperature. a, Schematic of a NW with labelled principal axes and PL-spectra measured with polarization angle parallel (x axis) and perpendicular (y axis) to the NW longitudinal direction. The polarization angle is measured in the x-y plane of the NW, parallel to the substrate. b, Polar plot of the linear polarization intensity of the laser emission

The wavelength tunability of the NW laser is an important motivation to explore the GaAsSb-based superlattice design and an important prerequisite for practical applications in the near-infrared wavelength region. By tuning the Sb compositional profile in the superlattices, either by the Sb flux or the GaAsSb growth time in the superlattices, the wavelength emission of the NW laser can be tuned from 890 nm to 990 nm, as shown in Fig. 4a. With a reduction of the Sb content by reducing the Sb flux, the lasing wavelength blue-shifts, leading to lasing emission around 890 nm with an Sb content of ~ 1 at. % in sample A as measured by EDX, shown in Fig. 4b. With higher Sb content in the GaAsSb superlattice, the lasing emission red-shifts. The longest wavelength lasing emission observed is at 990 nm (see Fig. 4d), which comes from the superlattice with the highest Sb content (sample C). ~ 8.0 at. % Sb was measured by EDX in sample C and it was obtained by doubling the GaAsSb potential well growth time as compared to sample B. It

should be noticed that for the NW superlattice structure with the lowest Sb content, the lasing is achieved at a much higher laser threshold (~ 12 kW cm^{-2}) compared to the NW lasers with higher Sb content. (see Supplementary Section X) This indicates that the room-temperature lasing threshold strongly depends on the Sb profile of the GaAsSb-based potential wells in the NW superlattices.[19]

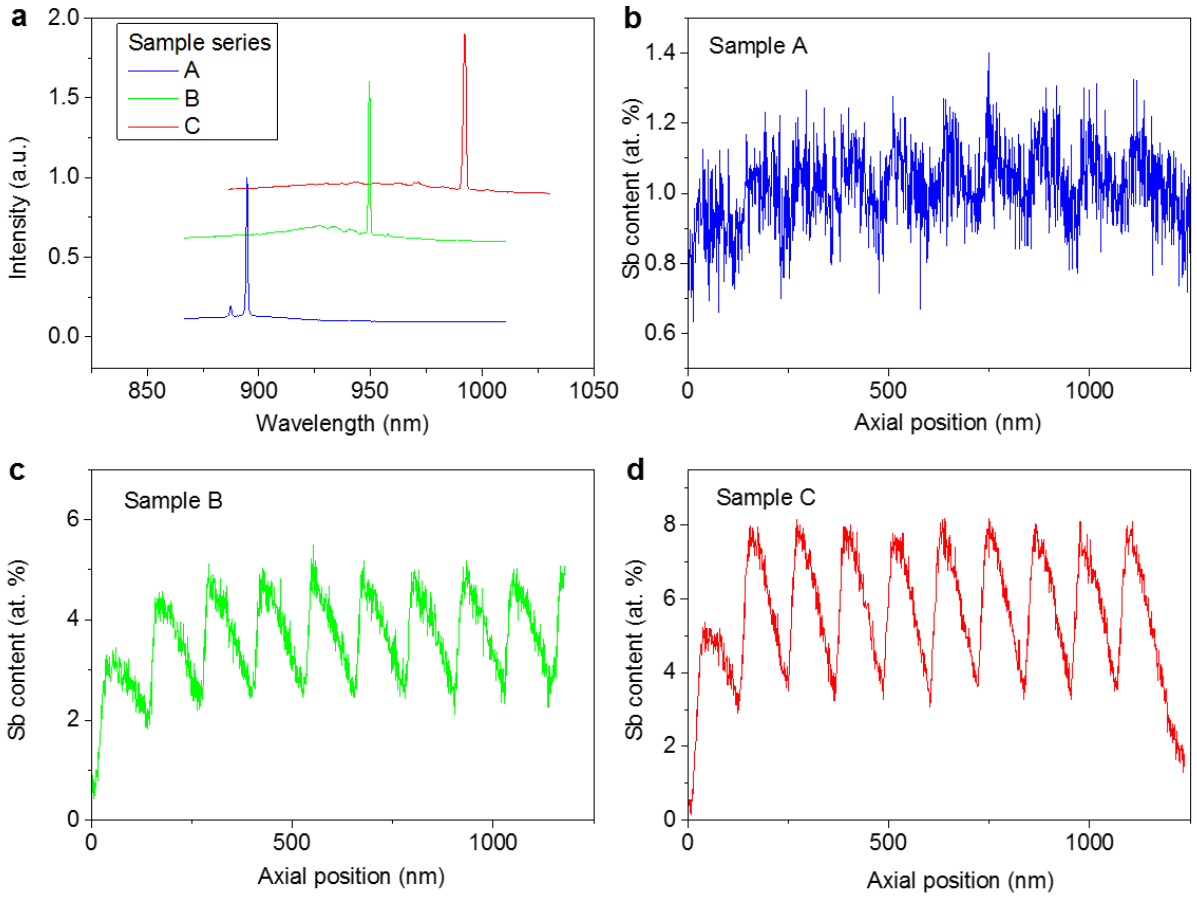

Figure 4. Laser emission spectra and Sb content profiles (at. %) for NW superlattice Samples A, B, and C. a, Laser emission tuned from around 890 nm (Sample A), 950 nm (sample B) to 990 nm (sample C) by controlling the Sb composition in the GaAsSb-based superlattices. b-d, Corresponding EDX Sb composition profiles from the 4th GaAsSb-based superlattice of Samples A, B and C, respectively.

To better understand the lasing mechanism from the NW superlattice lasers, gain simulations have been performed based on the compositional profiles of Sb in Fig. 1f (see Supplementary Section I and VIII). The electrons in the conduction band are shared among all GaAsSb potential wells in one superlattice due to the shallow conduction band potential, while the holes are confined in each GaAsSb quantum well in the valence band, at least for the highest-lying subbands. The length of the gain medium is estimated to be ~ 30 nm per GaAsSb-based quantum well in the superlattices, based on the overlap between the electron and hole wave functions in the fundamental subbands in the conduction and valence band, respectively. Due to the strong hole confinement, different GaAsSb-based quantum wells will contribute to the active medium gain independently. (For further explanations see Supplementary Section VIII). This correlates well with the Gaussian shape of the emission peak at the lasing threshold, which results from the electronic difference of the GaAsSb-based multiple quantum wells (see Supplementary Section V). The total material gain at lasing threshold is estimated to be ~ 3.1×10^3 cm^{-1} at room temperature from FDTD and material gain simulations. Although this room-temperature value is ~ 1.7 time higher than previously reported bulk-gain GaAs NW lasers[16,34], the length of the gain region is only one quarter of the bulk-gain NW laser. Compared to the bulk-gain NW structure, our NW superlattice structures have a much smaller gain volume without sacrificing the carrier collection efficiency, which significantly increases the carrier density in the active gain medium under the same optical pumping power.[35] This makes the population inversion in GaAsSb-based NW quantum wells easier than in a bulk-gain NW structure, and the lasing threshold is thus reduced. Moreover, our NW superlattice structure has a highly-repeatable well-controlled compositional profile and high radiative recombination rate, preventing severe band filling-induced blue-shifts below the lasing threshold and enabling lasing at longer near infrared

wavelengths with minimized re-absorption loss, which is very challenging in other NW laser architectures utilizing quantum confinement effects. Combining the characteristics of no band filling-induced blue-shift at room temperature with the mode filtering effect from the GaAs binary cavity[36], single-mode lasing operation at room temperature and at near-infrared wavelengths can be realized with the current NW superlattice structure. By further applying this architecture into other III-V materials systems, e.g. InAsP-based superlattices in InP NWs or InAsSb-based superlattices in InAs NWs, high-performance tunable lasing emission could possibly be achieved in much larger wavelength ranges from visible to far-IR.

In conclusion, we have presented the excellent lasing properties of GaAsSb-based NW superlattices. By adjusting the Sb-compositional profiles in the NW superlattices, single-mode laser emission wavelengths can be tuned from 890 nm to 990 nm at room temperature. Due to its unique superlattice design with efficient carrier collection and radiative recombination, the NW superlattices deliver unprecedented low-threshold 6 kW cm^{-2} (75 $\mu J/cm^2$ per pulse) and high Q factor lasing with a high characteristic temperature (~129 K). The NW superlattice structure thus provides a new concept for designing tunable and efficient NW laser sources, showing promise as a useful building block for future nanophotonic light sources and optical interconnects.

Methods NW growth: The GaAsSb-based NW superlattices were grown at a substrate temperature of 625 ˚C using a solid source MBE (Veeco GEN 930). The Ga and As_2 fluxes used in this study were 0.7 ML/s and 2.5×10^{-6} Torr, respectively. The growth of the NW array with superlattices were initiated by suppling a Ga flux for 45 s to form the Ga catalyst in the holes of the EBL-patterned oxide mask on a Si(111) substrate, and then a short (~ 100 nm) NW stem of GaAsSb were grown for 1 min with an Sb_2 flux of 1×10^{-7} Torr to improve the vertical yield in

the array. This is because Sb stabilizes the crystal in the zinc-blende phase, which prevents the formation of three-dimensional twinnings that leads to a reduced yield of vertical NWs. Subsequently, a GaAs NW segment was grown for 2 min before the growth of the GaAsSb-based NW superlattice. Each GaAsSb superlattice period in the six superlattices was grown by first keeping the Ga shutter closed and the Sb and As shutters open for 10 s (samples A and B) or 20 s (sample C), followed by 96 s with Sb shutter closed and Ga and As shutters open. The GaAs spacers between each superlattice were grown with Ga and As shutters open for 3 min. Sb_2 flux during superlattice growth was 0.3×10^{-6} Torr (sample A) or 1×10^{-6} Torr (samples B and C). The Ga catalyst solidification process was performed by supplying an As_2 flux of 1×10^{-5} Torr for 15 min, followed by the growth of an $Al_{0.33}Ga_{0.67}As$ shell (14 nm thick) and a GaAs cap (6 nm thick) to passivate NW surface states.

Electron microscopy: For the TEM characterization, the NW superlattice lasers were first transferred from the substrate to a 50 nm thick SiN window TEM grid using a diamond scraper. The NWs were characterized by conventional TEM using a JEOL JEM-2100F at 200 kV. For each of the three samples in this study, one structurally representative NW laser was selected to be thinned by FIB, using a FEI Helios NanoLab DualBeam, for a more detailed and compositional TEM study. The prepared TEM lamellas were ~ 12 μm long and ~ 100 nm thick and included the entire NW laser. The specimens were characterized with HAADF STEM and EDX using a JEOL JEM ARM200F at 200 kV with a Centurio SDD EDX system (solid angle 0.98 sr). EDX data were acquired with the NW laser specimen on the [112] zone-axis. For the quantitative analysis, the EDX data were first denoised using principal component analysis before a Cliff Lorimer based quantification routine was applied with calculated k-factors. All EDX data analysis was performed using the Python based library HyperSpy.

Optical spectroscopy: For the optical pumping experiments, the as-grown NW superlattice lasers were mechanically detached from the Si substrate using a sharp diamond-tip scriber and transferred to a SiO2/Si substrate with an oxide thickness of 300 nm. The optical pumping was achieved with a mode-locked Spectra Physics Tsunami Ti:Sapphire laser delivering 150 fs pulses at 800 nm with repetition rate of 80 MHz. Optical excitation and collection were done with a Mitutoyo 50× NA0.65 infinity corrected microscope objective (50 % transmission loss at the excitation wavelength). The beam spot was defocused to ~ 8 μm in order to excite most of the NW superlattices. The PL emission was dispersed with a Horiba Jobin-Yvon iHR500 spectrometer and detected with an Andor Newton electron multiplying (EM) CCD camera. The time-resolved PL (TRPL) data were acquired with an Optronis Optoscope SC-10 streak camera used in synchroscan mode, attached to a Princeton Instruments Acton SP2500 spectrograph. For the low temperature experiments, a Janis ST-500 optical cryostat was used. The CL was done in hyperspectral mode in a dedicated SEM with a cold stage (Liquid He, 8 K). The data was recorded with software from DELMIC, using an Andor Newton CCD, connected to a SPEX monochromator. The resolution of the spectrograph for the settings used in the optical pumping experiments was 0.51 nm (using a 300 lines/mm grating blazed at 800 nm, and an entrance slit width of 0.2 mm).

AUTHOR INFORMATION

Corresponding Author

*helge.weman@ntnu.no

Author Contributions

D.R. conceived the idea and designed the structures under supervision from B.O.F. and H.W.. D.R. carried out the growth experiments, SEM and preliminary TEM characterizations. D.R. and L.A.

performed the PL and optical pumping measurements. L.A. performed the electronic structure and gain simulations in cooperation with D.R.. J.S.N. carried out the TEM characterizations under supervision from A.T.J.v.H.. J.Y. performed the FDTD simulations under supervision from G.C.. A.G carried out the CL measurements. J.H. contributed with data analysis. D.R. wrote the manuscript with contributions from all authors. B.O.F. and H.W. supervised the project.

Notes

The authors declare no competing financial interest.

ASSOCIATED CONTENT

Supporting Information. The Supporting Information is available free of charge on the ACS Publications website at DOI: 10.1021/acs.nanolett.xxxxxxx. I. Lasing mechasim; II. Sb composition profiles in the NW superlattices; III. Guided mode simulation of the NW laser cavity; IV. Direct observation of Fabry–Pérot modes from CL; V. Lineshape fitting of optical emission. VI. Time-resolved PL experiments; VII. Low-temperature optical pumping experiments; VIII. Mode confinement factor and modal gain required for lasing; IV. Rate equation fitting; X. Optical pumping experiments on NW superlattices with different Sb compositions;

ACKNOWLEDGMENT

We would like to thank Tron Arne Nilsen and Dong-Chul Kim for their technical supports. This work was supported by the FRINATEK (Grant 214235) and NANO2021 (Grant 239206) programs of the Research Council of Norway. The Research Council of Norway is also acknowledged for the support to NTNU NanoLab through the Norwegian Micro- and Nano-Fabrication Facility, NorFab (197411), the NORTEM facility (197405) and the Norwegian PhD Network on

Nanotechnology for Microsystems (FORSKERSKOLER-221860). We also acknowledge the support from the Swedish Research Council (VR), the Foundation for Strategic Research (SSF), the Knut and Alice Wallenberg Foundation (KAW) and NanoLund. Jianfeng Yang would like to acknowledge the financial support from the China Scholarship Council (CSC, No. 201306070023).

REFERENCES

(1) Huang, M. H. *Science.* **2001**, *292*, 1897–1899.

(2) Johnson, J. C.; Choi, H.-J.; Knutsen, K. P.; Schaller, R. D.; Yang, P.; Saykally, R. J. *Nat. Mater.* **2002**, *1*, 106–110.

(3) Duan, X.; Huang, Y.; Agarwal, R.; Lieber, C. M. *Nature* **2003**, *421*, 241–245.

(4) Chen, R.; Tran, T.-T. D.; Ng, K. W.; Ko, W. S.; Chuang, L. C.; Sedgwick, F. G.; Chang-Hasnain, C. *Nat. Photonics* **2011**, *5*, 170–175.

(5) Li, K. H.; Liu, X.; Wang, Q.; Zhao, S.; Mi, Z. *Nat. Nanotechnol.* **2015**, *10*, 140–144.

(6) Frost, T.; Jahangir, S.; Stark, E.; Deshpande, S.; Hazari, A.; Zhao, C.; Ooi, B. S.; Bhattacharya, P. *Nano Lett.* **2014**, *14*, 4535–4541.

(7) Zhu, H.; Fu, Y.; Meng, F.; Wu, X.; Gong, Z.; Ding, Q.; Gustafsson, M. V.; Trinh, M. T.; Jin, S.; Zhu, X.-Y. *Nat. Mater.* **2015**, *14*, 636–642.

(8) Eaton, S. W.; Fu, A.; Wong, A. B.; Ning, C.-Z.; Yang, P. *Nat. Rev. Mater.* **2016**, *1*, 16028.

(9) Qian, F.; Li, Y.; Gradečak, S.; Park, H.-G.; Dong, Y.; Ding, Y.; Wang, Z. L.; Lieber, C. M.

Nat. Mater. **2008**, *7*, 701–706.

(10) Tatebayashi, J.; Kako, S.; Ho, J.; Ota, Y.; Iwamoto, S.; Arakawa, Y. *Nat. Photonics* **2015**, *9*, 501–505.

(11) Laming, R. I.; Farries, M. C.; Morkel, P. R.; Reekie, L.; Payne, D. N.; Scrivener, P. L.; Fontana, F.; Righetti, A. *Electron. Lett.* **1989**, *25*, 12–14.

(12) Romanos, G.; Nentwig, G.-H. *J. Clin. Laser Med. Surg.* **1999**, *17*, 193–197.

(13) Ding, J. X.; Zapien, J. A.; Chen, W. W.; Lifshitz, Y.; Lee, S. T.; Meng, X. M. *Appl. Phys. Lett.* **2004**, *85*, 2361.

(14) Zhang, Q.; Li, G.; Liu, X.; Qian, F.; Li, Y.; Sum, T. C.; Lieber, C. M.; Xiong, Q. *Nat. Commun.* **2014**, *5*, 4953.

(15) Chin, A. H.; Vaddiraju, S.; Maslov, A. V.; Ning, C. Z.; Sunkara, M. K.; Meyyappan, M. *Appl. Phys. Lett.* **2006**, *88*, 163115.

(16) Saxena, D.; Mokkapati, S.; Parkinson, P.; Jiang, N.; Gao, Q.; Tan, H. H.; Jagadish, C. *Nat. Photonics* **2013**, *7*, 963–968.

(17) Mayer, B.; Rudolph, D.; Schnell, J.; Morkötter, S.; Winnerl, J.; Treu, J.; Müller, K.; Bracher, G.; Abstreiter, G.; Koblmüller, G.; Finley, J. J. *Nat. Commun.* **2013**, *4*.

(18) Saxena, D.; Wang, F.; Gao, Q.; Mokkapati, S.; Tan, H. H.; Jagadish, C. *Nano Lett.* **2015**, *15*, 5342–5348.

(19) Arakawa, Y.; Sakaki, H. *Appl. Phys. Lett.* **1982**, *40*, 939–941.

(20) Stettner, T.; Zimmermann, P.; Loitsch, B.; Döblinger, M.; Regler, A.; Mayer, B.; Winnerl, J.; Matich, S.; Riedl, H.; Kaniber, M.; Abstreiter, G.; Koblmüller, G.; Finley, J. J. *Appl. Phys. Lett.* **2016**, *108*, 11108.

(21) Saxena, D.; Jiang, N.; Yuan, X.; Mokkapati, S.; Guo, Y.; Tan, H. H.; Jagadish, C. *Nano Lett.* **2016**, *16*, 5080–5086.

(22) Yan, X.; Wei, W.; Tang, F.; Wang, X.; Li, L.; Zhang, X.; Ren, X. *Appl. Phys. Lett.* **2017**, *110*, 61104.

(23) Loitsch, B.; Jeon, N.; Döblinger, M.; Winnerl, J.; Parzinger, E.; Matich, S.; Wurstbauer, U.; Riedl, H.; Abstreiter, G.; Finley, J. J.; Lauhon, L. J.; Koblmüller, G. *Appl. Phys. Lett.* **2016**, *109*, 93105.

(24) Schuster, F.; Kapraun, J.; Malheiros-Silveira, G. N.; Deshpande, S.; Chang-Hasnain, C. J. *Nano Lett.* **2017**, *17*, acs.nanolett.7b00607.

(25) Glas, F. *Phys. Rev. B* **2006**, *74*, 121302.

(26) de la Mata, M.; Magén, C.; Caroff, P.; Arbiol, J. *Nano Lett.* **2014**, *14*, 6614–6620.

(27) Gudiksen, M. S.; Lauhon, L. J.; Wang, J.; Smith, D. C.; Lieber, C. M. *Nature* **2002**, *415*, 617–620.

(28) Hocevar, M.; Immink, G.; Verheijen, M.; Akopian, N.; Zwiller, V.; Kouwenhoven, L.; Bakkers, E. *Nat. Commun.* **2012**, *3*, 1266.

(29) Ren, D.; Dheeraj, D. L.; Jin, C.; Nilsen, J. S.; Huh, J.; Reinertsen, J. F.; Munshi, A. M.; Gustafsson, A.; van Helvoort, A. T. J.; Weman, H.; Fimland, B.-O. *Nano Lett.* **2016**, *16*,

1201–1209.

(30) Ren, D.; Huh, J.; Dheeraj, D. L.; Weman, H.; Fimland, B.-O. *Appl. Phys. Lett.* **2016**, *109*, 243102.

(31) Li, L.; Pan, D.; Xue, Y.; Wang, X.; Lin, M.; Su, D.; Zhang, Q.; Yu, X.; So, H.; Wei, D.; Sun, B.; Tan, P.; Pan, A.; Zhao, J. *Nano Lett.* **2017**, *17*, 622–630.

(32) Yuan, X.; Saxena, D.; Caroff, P.; Wang, F.; Lockrey, M.; Mokkapati, S.; Tan, H. H.; Jagadish, C. *J. Phys. Chem. C* **2017**, *121*, 8636–8644.

(33) Ho, J.; Tatebayashi, J.; Sergent, S.; Fong, C. F.; Iwamoto, S.; Arakawa, Y. *ACS Photonics* **2015**, *2*, 165–171.

(34) Chen, S.; Jansson, M.; Stehr, J. E.; Huang, Y.; Ishikawa, F.; Chen, W. M.; Buyanova, I. A. *Nano Lett.* **2017**, *17*, 1775–1781.

(35) Li, C.; Wright, J. B.; Liu, S.; Lu, P.; Figiel, J. J.; Leung, B.; Chow, W. W.; Brener, I.; Koleske, D. D.; Luk, T.-S.; Feezell, D. F.; Brueck, S. R. J.; Wang, G. T. *Nano Lett.* **2017**, *17*, acs.nanolett.6b04483.

(36) Zhang, C.; Zou, C.-L.; Dong, H.; Yan, Y.; Yao, J.; Zhao, Y. S. *Sci. Adv.* **2017**, *3*.

TOC